

Cite this: *Energy Adv.*, 2023,  
2, 54

# Recent ReaxFF MD studies on pyrolysis and combustion mechanisms of aviation/aerospace fuels and energetic additives

Menghui Chen,<sup>†a</sup> Wei Li,<sup>†b</sup> Houjun Zhang,<sup>a</sup> Menghui Liu,<sup>a</sup> Jinli Zhang,<sup>ib a</sup>  
Xiangyuan Li<sup>ib c</sup> and You Han<sup>ib \*a</sup>

Development of aviation and aerospace fuels requires deep insight into the pyrolysis and combustion mechanisms. However, rapid and complex reactions during fuel combustion make it difficult to accurately describe the free radicals, reaction paths and other relevant details in large-scale reaction systems through experiments or quantum mechanics. The molecular dynamics (MD) simulation based on reaction force-fields (ReaxFF) is an effective method to solve the above problems, which can reveal the overall reaction mechanism in the fuel combustion process by dynamically describing the breakage and formation of bonds. Here in, the recent progress of ReaxFF MD in exploring the pyrolysis and combustion mechanism of aviation fuels, aerospace fuels and energetic additives is summarized, especially for aviation kerosene model substitutes, high-density aviation fuels, aerospace fuels and energetic additives under various conditions. Finally, the shortcomings of ReaxFF MD simulation in describing fuel pyrolysis or combustion systems are discussed, and the application prospect of ReaxFF MD simulation in the fuel field is prospected.

Received 20th October 2022,  
Accepted 27th November 2022

DOI: 10.1039/d2ya00285j

rsc.li/energy-advances

## 1 Introduction

The construction of a reasonable physical model and chemical kinetic mechanism of aviation and aerospace fuels will help researchers to deepen their understanding of the pyrolysis and combustion process of aerospace fuel, and then play a guiding role in engine design and optimization. Researchers have proposed a large number of physical replacement models<sup>1–3</sup> and related chemical mechanisms for aviation fuel through experimental studies.<sup>4,5</sup> These studies enable people to understand the thermophysical and thermochemical properties of aviation fuel, but there is still a lack of details about the fuel reaction path and free radicals in the combustion process. At this extreme temperature and pressure, chemical reactions take place in picoseconds and the reaction paths are coupled, which brings great difficulties to the detection of free radicals, intermediates and reaction paths; even with the latest instruments, it is difficult to capture them completely.<sup>6</sup> However, the development of computational chemistry makes up for the shortcomings of experiments.

Quantum chemical (QC) simulation is a widely used molecular simulation method based on quantum mechanics (QM). It obtains a high-precision solution at the electronic scale by solving the Schrödinger equation, which allows it to accurately predict the potential barrier of the reaction.<sup>7,8</sup> However, the high computational cost limits the quantum chemical simulation to the simple system of small molecules and picosecond time scale. In addition, the defect of the preset reaction path makes this simulation method unsuitable for complex macromolecular systems such as coal and biomass. The molecular dynamics (MD) simulation method can calculate the trajectory of atoms by solving Newtonian equations, which makes it possible to apply it in large-scale systems<sup>9</sup> with lower cost and shorter time than quantum chemical simulation methods. However, it is worth noting that molecular dynamics simulation is lacking in the study of chemical reaction processes, which limits its further application.

Quantum chemical simulation and molecular dynamics simulation have their strengths and weaknesses, and the urgent need to study large-scale reaction systems promotes their integration, thus developing a new simulation method – reaction molecular dynamics simulation method. The ReaxFF reaction force field developed by van Duin *et al.*<sup>10</sup> expresses bond length in terms of bond order. Based on this method, ReaxFF can dynamically describe the breakage and formation of bonds in the reaction process. And in this process, a smooth

<sup>a</sup> School of Chemical Engineering and Technology, Tianjin University, Tianjin 300072, China. E-mail: yhan@tju.edu.cn<sup>b</sup> Science and Technology on Aerospace Chemical Power Laboratory, Hubei Institute of Aerospace Chemotechnology, Xiangyang 441003, China<sup>c</sup> School of Chemical Engineering, Sichuan University, Chengdu 610065, China

† These authors contributed equally to this work.



and continuous transition can be achieved between non-bonded states and bond states without the existence of energy or force discontinuities. The ReaxFF potential parameters are optimized by the data obtained from experiments and quantum chemistry calculations, which makes the ReaxFF MD simulation close to the accuracy of quantum chemistry calculations. The same calculation method as molecular dynamics simulation makes ReaxFF MD simulation several orders of magnitude faster than quantum chemistry calculation, which greatly reduces the cost. More importantly, ReaxFF MD simulation does not rely on prior chemical knowledge, which makes it widely used in complex reaction systems such as coal,<sup>11</sup> biomass,<sup>12</sup> and fuel.<sup>13</sup>

The application of ReaxFF is closely related to the development and improvement of its reaction force field. As one of the earliest branches of ReaxFF, the reaction force field related to the combustion branch<sup>14</sup> has been continuously updated and expanded in recent years. In order to study the initial reaction of the hydrocarbon gas phase at high temperature, Chenoweth *et al.*<sup>15</sup> developed the CHO-2008 force field by adding the transition state information and relevant quantum mechanical data during hydrocarbon oxidation to the initial training set of hydrocarbons. And the CHO-2008 force field was used for methane, propylene, *o*-xylene and benzene oxidation systems, and achieved satisfactory results. So far, the CHO-2008 force field is still one of the most widely used reaction force fields.<sup>16–19</sup> Ashraf *et al.*<sup>20</sup> developed the CHO-2016 force field based on the CHO-2008 force field, improving the range of applications and simulation accuracy of ReaxFF. Compared to the CHO-2008 force field, the CHO-2016 force field maintains the prediction accuracy of the CHO-2008 force field for large hydrocarbons. On this basis, the CHO-2016 force field provides a richer set of radicals and reaction pathways, systematically improving on the lack of prediction accuracy of the CHO-2008 force field in describing the oxidation of small hydrocarbons to carbon dioxide. In addition, the shortcomings of the CHO-2008 force field regarding the overprediction of the rate of hydrogen extraction by oxygen and thus the underestimation of the initial temperature of hydrocarbon oxidation have been effectively addressed. In order to explore the combustion of hydrogen at low temperature and high pressure, Cheng *et al.*<sup>21</sup> developed the OH-2014 force field, which improved the lack of prediction of H<sub>2</sub>O and other intermediates in the CHO-2008 force field, and provided a feasible tool for studying the reaction mechanism of H<sub>2</sub> at real temperature. In addition, they have developed adaptive Accelerated ReaxFF Reaction Dynamics by combining reaction molecular dynamics with acceleration dynamics and have tested a hydrogen combustion system using the HO-2014 force field to achieve satisfactory results at a low cost. They showed that this approach may have significant advantages in the future for describing longer reaction systems at lower temperatures. Kowalik *et al.*<sup>22</sup> have added a parametric description of the N atom to the CHO-2016 force field, resulting in the development of a CHON-2019 force field that is more suitable for probing the specific details of the transformation of polymers into carbon fiber structures. They explored the formation kinetics of N<sub>2</sub> and its interaction with related free radicals during the carbonization of polymers using the improved CHON-2019 force

field, determining the formation path of all-carbon rings, and put forward new insights into understanding how polymers evolve into graphene structures. ReaxFF has absorbed a large amount of metal<sup>23–25</sup> and non-metallic elements<sup>26,27</sup> in the process of continuous application to new fields, and developed a large number of force fields, which makes it applicable in most scientific research fields.

During the simulation of ReaxFF MD, specific parameter settings such as temperature, pressure and time step affect the results of the simulation. In view of the cost of the simulation, ReaxFF MD is generally set at a much higher temperature than the experimental temperature, but numerous studies have shown that an increase in temperature only accelerates the reaction and has a small effect on the reaction process, and the simulation results are in qualitative agreement with the experimental values. The effect of pressure on the reaction process is not as significant as that of temperature, but an increase in pressure increases the probability of molecular collisions, which also has an accelerating effect on the reaction process. However, given the stability of the system, the pressure is generally only set when simulating larger reaction systems. The choice of time step determines the accuracy of the simulation results. Jensen *et al.*<sup>28</sup> explored the effect of time step setting on the reaction by testing six carbon-based molecules using different time steps. The results showed that smaller time steps were required at higher temperatures to obtain accurate simulation results. The Chenoweth parameter is sufficient for accurate simulations at temperatures below 3000 K with a time step of 0.1 fs. At present, most of the studies on the molecular dynamics of fuel pyrolysis and combustion use this time step (0.1 fs).

Recent articles<sup>14,29–31</sup> provide a comprehensive review of the development of ReaxFF and its applications in various fields. However, these articles are too sketchy in describing the reaction mechanism of the pyrolysis and combustion of aviation fuel. Moreover, there are few studies on the pyrolysis and combustion mechanism of aerospace fuels and their energetic additives. Therefore, this review intends to sort out the studies on the application of ReaxFF in exploring the reaction mechanism of pyrolysis or combustion of aviation fuels, aerospace fuels and energetic additives. In the second part, the progress of using ReaxFF to study the pyrolysis and combustion mechanism of aviation kerosene model substitutes and high-density aviation fuels is introduced. In the third part, the use of ReaxFF in exploring the pyrolysis and combustion mechanism of aerospace fuels and energetic additives is introduced. Finally, the content of the full text is summarized, the shortcomings of ReaxFF are discussed and the development of ReaxFF is prospected.

## 2 Pyrolysis and combustion mechanism of aviation fuels

The study of single component pyrolysis systems with ReaxFF MD provides comprehensive and unobtrusive information on the mechanism of component pyrolysis and reaction products. These chain, cycloalkane and aromatic hydrocarbon components



are the basis for the model compounds of aviation paraffin. The study of these single components has provided a wealth of information that has led to a better understanding of the overall mechanism of aviation paraffin combustion. In contrast to single-component pyrolysis, radicals, intermediates and other species formed by the first component to be pyrolysed in multi-component pyrolysis may attack other reactant molecules, causing changes in the reaction pathway and thus affecting the reaction mechanism and products. A comparison of multi-component and single-component pyrolysis systems can demonstrate the differences between the two and thus reveal the influence of the interaction of the different components on the reaction process and improve the understanding of the overall mechanism of aerospace paraffin combustion. Overall, the combination of the single- and multi-component models of ReaxFF MD provides a clearer and more comprehensive picture of the overall reaction mechanism of aviation kerosene and provides a basis and guidance for the design and optimisation of engines.

## 2.1 One-component pyrolysis and combustion mechanism of aviation fuels

The general fuels currently used in domestic and foreign aviation fields are RP-3 and Jet A/Jet A-1 series kerosene. The research on the combustion mechanism of real aviation kerosene at high temperature can provide a reference for the optimization and improvement of the engine. However, considering the complexity of the composition of real aviation fuel, this is an almost impossible task. Therefore, the alternative model selected based on the physical and chemical properties of aviation kerosene has become an acceptable solution for the research of aviation kerosene. A large number of researchers have proposed different multi-component aviation kerosene substitution models, such as the four-component RP-3 aviation kerosene substitution model proposed by Yu *et al.*,<sup>32</sup> the three-component Jet A-1 aviation kerosene substitution model proposed by Dagaut *et al.*,<sup>33</sup> the three-component Jet A aviation kerosene substitution model proposed by Dooley *et al.*<sup>34</sup> and so on. Although there are a variety of alternative models for aviation kerosene, most of them include alkanes, naphthenes and aromatic hydrocarbons. And undisturbed kinetics and reaction mechanism can be obtained by simulating these components separately. These works, combined with the research of multi-component models, can provide a clearer and more comprehensive understanding of the reaction mechanism of aviation kerosene.

**2.1.1 Pyrolysis and combustion mechanism of alkanes in aviation fuels.** The most commonly used alkanes in aviation kerosene substitution models are *n*-octane,<sup>5</sup> isooctane,<sup>34</sup> *n*-decane,<sup>33,34</sup> *n*-dodecane,<sup>5,32</sup> and *n*-hexadecane.<sup>5</sup> Several studies are devoted to revealing the pyrolysis and combustion mechanism of these basic components of aviation fuel.

Liu *et al.*<sup>35</sup> explored the thermal decomposition mechanism of *n*-octane in the liquid state, the effect of temperature and the formation mechanism of three main thermal decomposition products through reaction molecular dynamics and density functional theory calculation. Eight thermal decomposition

paths of *n*-octane were determined and it was found that the end of the *n*-octane molecule was not easy to react, and the increase of temperature greatly promoted the reaction. The major products, H<sub>2</sub> and CH<sub>4</sub>, are mainly from the attack of H and CH<sub>3</sub> free radicals and the binding reaction between free radicals. On the other hand, ethylene mainly comes from  $\beta$ -scission reactions of macromolecules. Wang *et al.*<sup>36</sup> applied the optimized reaction force field to the pyrolysis of isooctane, and they used a time step of 0.1 fs in the simulation, which showed that the cleavage path of the C–C bond connected to quaternary carbon occupies the highest proportion in the pyrolysis path of isooctane. And it can be observed from the number of isooctane pyrolysis products and intermediates that C<sub>2</sub> species play an important role in the pyrolysis of isooctane. Liu *et al.*<sup>37</sup> investigated and compared the combustion mechanism, reaction performance and coking status of six octane isomers. The results show that both *n*-octane and isooctane undergo the stage of isomerization during combustion, but the activity of isooctane decreases due to the existence of a branched chain compared with *n*-octane, and the trend of coking is obvious with the increase of the branched chain.

Liu *et al.*<sup>38</sup> simulated the pyrolysis process of *n*-decane and focused on the formation of soot nanoparticles during the pyrolysis of *n*-decane. The results show that the dissociation energy of the C<sub>2</sub>–C<sub>3</sub> bond of the *n*-decane molecule is the lowest, and the cleavage of the C<sub>2</sub>–C<sub>3</sub> bond is the most likely path for the decomposition of the *n*-decane molecule. In addition, it is also found that the formation of soot nanoparticles needs to go through four stages: initial carbon ring formation, polycyclic aromatic hydrocarbon (PAH) growth, PAH aggregation nucleation and carbon core surface growth, as shown in Fig. 1(a). Zhou *et al.*<sup>39</sup> explored the decomposition process of *n*-decane under the action of an electric field. The decomposition pathway and proportion distribution of *n*-decane are shown in Fig. 1(b). The study found that the electric field enhanced the polarization of *n*-decane at low temperature. It also significantly promoted the decomposition of *n*-decane, and the number of PAHs was significantly reduced during the decomposition of *n*-decane, as shown in Fig. 1(c). These works provide a reference for the development of anti-coking methods in the combustion process of aviation fuel. Wang *et al.*<sup>40</sup> tested the effects of several additives on the pyrolysis of *n*-decane and it was found that 1-nitropropane greatly reduces the decomposition and activation energy of reaction molecules during the pyrolysis of *n*-decane, and thus plays the highest role in promoting the pyrolysis of *n*-decane. This work provides a reference precedent for the screening of fuel additives.

Wang *et al.*<sup>18</sup> simulated the pyrolysis and combustion process of *n*-dodecane. The results show that the pyrolysis path of *n*-dodecane is C–C bond breakage, dehydrogenation and H extraction of small molecular free radicals. In addition, it is also found that the effect of density/pressure on the pyrolysis of *n*-dodecane is not as significant as that of temperature and there is a threshold for the effect of density/pressure on pyrolysis. The importance of formaldehyde molecules can be observed from the oxidation simulation process of *n*-dodecane,





Fig. 1 (a) Mechanism of soot formation by pyrolysis of *n*-heptane at 3000 K;<sup>38</sup> (b) initial pyrolysis path and proportion of *n*-decane under an electric field;<sup>39</sup> and (c) the largest molecule structure evolution during the reaction process.<sup>39</sup>

which is consistent with the existing kinetic models. The common reactive molecular dynamics studies of fuel combustion properties are carried out at high temperatures, but these temperatures deviate from the temperature for practical industrial applications. To obtain atomic-scale information of fuel combustion processes at industrially relevant temperature and time scales, Bal *et al.*<sup>41</sup> studied the pyrolysis and oxidation of *n*-dodecane at low temperature to 700 K and ultra-long time to 39 seconds by collective variable driven super dynamics (CVHD<sup>42</sup>). The simulation results are consistent with the previous studies. This work provides a reference for exploring the reaction mechanism of reaction molecular dynamics under experimental conditions.

Chen *et al.*<sup>43</sup> studied the pyrolysis process of *n*-hexadecane at high temperature, which showed that the eight pyrolysis paths of *n*-hexadecane involved C–C bond breakage, and the existence of double free radicals accelerated the reaction during the pyrolysis of *n*-hexadecane. In addition, the optimum conditions for the pyrolysis of *n*-hexadecane to ethylene and hydrogen were determined by exploring the effects of temperature and pressure on the pyrolysis process. Subsequently, the research group<sup>44</sup> further studied the pyrolysis process of *n*-hexadecane under the action of three kinds of catalysts. The results showed that the introduction of hydroxyl groups on the surface of the catalyst was beneficial to the increase of ethylene production. On the other hand, the addition of aluminum stabilized the structure of the catalyst, promoting the dehydrogenation of reactant molecules and inhibiting the formation of the C–O bond. These works provide a reference for the application of heavy hydrocarbons in industry.

As the most basic component of aviation fuels, the research work on the pyrolysis and oxidation mechanism of endothermic hydrocarbon fuel saturated alkanes provides an opportunity to deeply understand the ignition and combustion properties of aviation fuel, further achieve full combustion and avoid coking of aviation fuel in the engine.

**2.1.2 Pyrolysis and combustion mechanism of naphthenic hydrocarbons in aviation fuels.** Naphthenes have become one of the indispensable model substitutes for describing aviation fuels because of their unique properties. Cyclohexane and its derivatives are widely used in many aviation kerosene model substitutes.<sup>45,46</sup> Naphthenes have received extensive attention due to their high content in practical fuels and some works have been done on naphthene pyrolysis<sup>47–52</sup> and combustion.<sup>53</sup>

Liu *et al.*<sup>47</sup> studied the detailed pyrolysis process of methylcyclohexane and found that there are four initial decomposition paths of methylcyclohexane, as shown in Fig. 2(a). It can be observed that the first type of reaction  $C_7H_{14} \rightarrow \cdot C_7H_{14} \cdot$  has the highest proportion. It can be seen from Fig. 2(b) that the main product (*i.e.*,  $C_7H_{14}$  double radical) is further decomposed to produce ethylene and propylene, which is different from the previous study. Another work<sup>50</sup> studied the pyrolysis mechanism of methylcyclohexane in the presence of suspended functional fossil graphene tablets (FGS). As shown in Fig. 2(c), the functional groups on FGS significantly reduce the potential barrier of methylcyclohexane dehydrogenation, accelerate the decomposition of reaction molecules and produce more small molecular free radicals, thus increasing the conversion of methylcyclohexane to low-carbon species. Liu *et al.*<sup>53</sup> further studied the oxidation process of methylcyclohexane and clarified the oxidation mechanism of methylcyclohexane. Through the research, they found a new fuel consumption route in which methylcyclohexane is isomerized first and then decomposed into small molecular olefins. In addition, they also determined the important role of intermediates  $CH_2O$  and  $H_2O_2$  in the product formation process. Another study<sup>52</sup> reveals the growth of polycyclic aromatic hydrocarbons (PAHs) during *n*-hexane combustion. The research results show that the formation of PAHs involves the process of entanglement of long carbon chains into rings and growth by molecular chain attachment. In addition, the optimal temperature range for the growth of PAHs has also been found





Fig. 2 (a) Four decomposition paths of methylcyclohexane and their proportion,<sup>47</sup> (b) the formation route for the main products of methylcyclohexane,<sup>47</sup> and (c) reaction barriers for the dehydrogenation of MCH with and without added FGS containing an oxygen functional group.<sup>50</sup>

through research. These works enrich the data of high temperature cracking or oxidation of cycloalkanes and provide support for the establishment of the overall reaction mechanism and kinetic model of cycloalkanes.

**2.1.3 Pyrolysis and combustion mechanism of aromatic hydrocarbons in aviation fuels.** Aromatic hydrocarbons are very common in the alternative model<sup>32–34</sup> of aviation kerosene. In order to understand the properties of aromatic hydrocarbons more comprehensively, the process of pyrolysis or combustion of aromatic hydrocarbons has been studied<sup>17,54–61</sup> under various conditions.

Cheng *et al.*<sup>17</sup> explored the oxidation process of toluene and found three paths for the initial reaction of toluene, namely, (1) dehydrogenation of toluene induced by oxygen and other small molecular free radicals, (2) the cleavage of the C–H bond of methyl to benzyl, and (3) the cleavage of the C–C bond of methyl to benzene to form phenyl. In these three paths, the first reaction mainly occurs when oxygen is sufficient, and the proportion of the other two reactions increases when oxygen is insufficient. Tan *et al.*<sup>58</sup> explored the effect of an applied electric field on the oxidation of toluene, and the results show that the electric field significantly promoted the oxidation process of toluene, so that toluene reacted at 2100 K where no reaction had occurred before. And the oxidation rate of toluene at 2100 K is consistent with the oxidation rate at 2900 K without an electric field. In addition, the authors also studied the effect of the electric field on the initial oxidation path of toluene. The results show that although the electric field promoted the formation of initial radicals and made toluene decompose faster, the effect of the electric field on the two reaction paths seemed to be indistinguishable. Finally, the authors further show that the electric field does not take into account the possible effect of the reaction molecular

polarization, which may cause the simulation results to deviate from the correct value. The authors suggest that researchers take note of this in subsequent studies. Fu *et al.*<sup>59</sup> then evaluated the effect of an external electric field on the oxidation and pyrolysis of toluene. The results showed that the electric field promoted the oxidation of toluene but did not significantly promote the pyrolysis of toluene. The internal reason was that the electric field increased the entropy change of the reactants and transition state, but the pyrolysis of toluene was driven by heat, so the effect was not obvious. These works are helpful to deepen people's understanding of the mechanism of pyrolysis and oxidation of toluene.

Wei *et al.*<sup>54</sup> studied the oxidation of benzene molecules on palladium nanoparticle catalysts. Fig. 3(a) shows the detailed process of benzene molecules being oxidized by palladium nanoparticles. As shown in Fig. 3, benzene molecules are first adsorbed on palladium nanoparticles, and then benzene molecules get rid of hydrogen atoms through several steps to form  $C_6H$ , which is oxidized to form an important intermediate  $C_6HO$ .  $C_6HO$  is further oxidized to form small molecular species, and the path is shown in Fig. 3(b). Statistical analysis of the ring-opening path shows that the ring-opening reaction of  $C_6HO$  occurs at oxygen-containing sites in 88% of cases. Further study revealed the detailed path of  $C_6HO$  oxidation, and demonstrated that the core substance of the  $C_6HO$  oxidation process is C2 species, and the final oxidation product is  $CO_2$ . This work provides an idea for the study of the oxidation mechanism of benzene molecules in the presence of catalysts.

Another study conducted by Qian *et al.*<sup>55</sup> explored the cause of explosion caused by the mixing of hydrogen peroxide and 1,3,5-trimethylbenzene (TMB). The study shows that the explosion process can be divided into two parts. First,  $H_2O_2$  due to its instability decomposes into OH and OOH free





Fig. 3 (a) The oxidation process of  $C_6H_6$  on Pd nanoparticles and (b) further oxidation of  $C_6HO$  to small molecules.<sup>54</sup>

radicals, and the hydrogen extraction reaction and binding reaction caused by the attack of the OH radical on TMB molecules lead to the cracking of the benzene ring. Subsequently, the small molecular species formed by TMB decomposition undergo further oxidation reaction. A huge amount of heat is released, causing the risk of explosion. This study confirmed that the existence of OH free radicals determines the speed of the whole reaction process, and controlling the number of OH free radicals can effectively reduce the risk of explosion. This work provides inspiration for the development of further explosion suppression methods in similar systems.

Chaudret *et al.*<sup>62</sup> studied the initial reaction paths of naphthalene and mono naphthalene and dimethyl naphthalene and the formation of coke molecules. It is revealed that the initial reaction paths of these substances are hydrogen dissociation and the reversed radical disproportionation mutation, and the position and number of methyl substituents will affect the kinetics and thermodynamics of the reaction. These results are supported by quantum mechanics. In addition, the formation of coke molecules involves the activation of the naphthalene derivative, dimerization or trimerization to form low molecular weight coke molecules, and condensation to form high molecular weight coke molecules. The information

about the pyrolysis mechanism of complex aromatic hydrocarbon molecules, the effect of the number and position of substituents on pyrolysis, and the formation process of coke molecules obtained in this work provide a reference for the study of complex aromatic hydrocarbon molecules.

## 2.2 Pyrolysis and combustion mechanism of multi-components of aviation fuels

The study<sup>63–70</sup> of the aviation kerosene multi-component or alternative model can provide information on the influence of multi-component interaction on the overall fuel combustion, and then help improve the combustion kinetic model and mechanism of aviation kerosene.

Song *et al.*<sup>69</sup> investigated the effect of mixing ratio on the mixed oxidation of toluene and *n*-decane. Compared with the single-molecule oxidation simulation, the initial reaction pathway of *n*-decane was not affected in the mixed oxidation simulation, while the oxidation pathway of toluene was changed. This is mainly because compared with toluene, *n*-decane is more likely to react when heated, and then a large number of highly reactive radicals are generated, which changes the oxidation path of toluene. The effect of H/C ratio on the representative intermediate HCHO was further discussed. The results show that the existence



time of HCHO decreased with the increase of H/C ratio at low temperature. However, at high temperature, the H/C ratio has almost no effect on HCHO. This phenomenon is primarily because the H/C ratio affects the generation of OH radicals, while the consumption of HCHO is dominated by OH and O<sub>2</sub>. This work shows the important influence of the H/C ratio on fuel oxidation, and provides guidance for the selection of various components in aviation kerosene. Liu *et al.*<sup>66</sup> simulated the combustion process of the model substitute of aviation kerosene JP8-1 composed of *n*-dodecane, *n*-tetradecane, isooctane, methylcyclohexane, *m*-xylene and tetralin, and explored the combustion mechanism and kinetics of JP8-1 aviation fuel. Table 1 lists the details of the alternative components and the path and combustion rate of the initial reaction. As shown in Table 1, the initial reaction paths of most components are consistent with the single-component simulation, mainly the C–C bond cleavage reaction, the C–H bond cleavage reaction, and the decomposition reaction caused by the attack of active free radicals. The kinetic analysis showed that the reaction rate of *n*-alkanes was the highest, followed by that of isooctane and methylcyclohexane, while the reaction rate of aromatics was the lowest, and the reaction rate of similar components decreased with the increase of molecular weight. The analysis of the formation path of coke molecules shows that ternary rings, five-membered rings and six-membered rings may be the precursors for the formation of coke molecules. This work provides insights for further understanding the combustion properties of JP8-1 and designing new and more reasonable model substitutes.

Zhao *et al.*<sup>63</sup> used reaction molecular dynamics to evaluate the difference in combustion between RP-3 aviation kerosene 3-component and 4-component model substitutes and the 45-component real model. A time step of 0.1 fs was used in the simulation. The results show that in terms of combustion kinetics, the 3-component and 4-component models have a relatively high pre-exponential factor and reaction activation energy than the 45-component models, which explains the higher reaction rate of the

3-component and 4-component models at high temperature. In terms of the formation of the main products, the three-component and four-component model substitutes showed a higher ethylene production rate, and more propylene was produced in the combustion products of the three-component model substitutes. This is caused by the higher content of *n*-alkanes in the two model substitutes and the large amount of 1,3,5-methylcyclohexane in the three-component model substitutes. This work shows the influence of the difference in fuel molecular structure and component content on the combustion mechanism and kinetics of fuel, and further deepens the understanding of the internal reasons for the reaction difference of model substitutes. It provides a reference for obtaining a more reasonable aviation kerosene substitution model through design optimization.

A study by Han *et al.*<sup>68</sup> used reactive molecular dynamics combined with machine learning to take the chemical composition content in the RP-3 model surrogate as the independent variable and the chemical reactivity data as the dependent variable. The RP-3 alternative model with higher reactivity can be obtained by optimizing the content of each component in the RP-3 alternative model. Through the error evaluation results, the best LightGBM machine learning model was selected among the three machine learning models of LR, SVR and LightGBM, and the component content of the substitute model compound was optimized by this model, and an improved three-component model was finally obtained. The rationality of the improved model is confirmed by the experimental results of ignition delay time. This study provides guidance for fine-tuning component fractions in aviation kerosene model compounds to obtain more reasonable surrogate models.

### 2.3 Pyrolysis and combustion mechanism of high-density aviation fuels

High-density aviation fuels used in scramjets have recently been extensively studied based on the need for higher Mach-

Table 1 Detailed information on surrogate components of JP8-1<sup>66</sup>

Name	Reaction	Snapshot	Type	$k'$
<i>n</i> -Dodecane	$C_{12}H_{26} \rightarrow \bullet C_6H_{13} + \bullet C_6H_{13}$		Normal-paraffin	$3.81 \times 10^5$
<i>n</i> -Tetradecane	$C_{14}H_{30} \rightarrow \bullet C_7H_{15} + \bullet C_7H_{15}$		Normal-paraffin	$3.5 \times 10^5$
Isooctane	$C_8H_{18} \rightarrow \bullet CH_2CH(CH_3)_2 + \bullet C(CH_3)_3$		Branched-paraffin	$2.96 \times 10^5$
Methylcyclohexane			Cyclo-paraffin	$1.01 \times 10^5$
<i>m</i> -Xylene			Monocyclic-aromatic	$5.32 \times 10^3$
Tetralin			Bicyclic-aromatic	$2.32 \times 10^2$



number flight speeds for aircraft. There has been a lot of work on high-energy density aviation fuel synthesis,<sup>71</sup> experimental research<sup>72–74</sup> and quantum mechanics research.<sup>74–76</sup> At the same time, research on the pyrolysis or oxidation mechanisms of high-density aviation fuels by using reactive molecular dynamics is also steadily progressing.

JP-10 is a kind of high-density hydrocarbon propellant with *exo*-tetrahydrodicyclopentadiene (*exo*-THDCPD) as the main body. JP-10 is the standard fuel of supersonic cruise missile because of its high density, high energy and high thermal stability. The small-scale molecular dynamics simulation of JP-10 has deepened people's understanding of the pyrolysis



Fig. 4 (a) Three stages of pyrolysis of JP-10 molecules.<sup>19</sup> (b) Pyrolysis and oxidation of JP-10 molecules on functionalized graphene sheets (FGS).<sup>78</sup>



and combustion mechanism of JP-10. Chenoweth *et al.*<sup>13</sup> identified two paths for the initial decomposition of JP-10 by single molecule simulation, that is, (1) JP-10 molecule loses ethylene to form cyclooctadiene, and (2) JP-10 undergoes cleavage to produce 1,4-pentadiene and cyclopentene. To obtain the complete reaction kinetics and mechanism of JP-10, Liu *et al.*<sup>19</sup> performed a large-scale simulation of JP-10 using a time step of 0.1 fs. The results show that the pyrolysis of JP-10 mainly has three stages, as shown in Fig. 4(a). JP-10 first undergoes ring-opening reaction in the first stage to form four kinds of double radicals, and then these four kinds of double radicals are further decomposed to form eight kinds of products. In the second stage, the products formed in the previous stage mainly undergo  $\beta$ -scission reactions to form free radicals. Then, the free radicals are further propagated through  $\beta$ -scission reactions or C–H bond cleavage reaction, and finally the chain termination reaction occurs in the third stage to form stable small molecular products.  $C_5H_7$  and  $C_3H_5$  radicals play an important role in the whole reaction stage. This work shows that ReaxFF can be used to explore large-scale reaction systems and obtain complete reaction mechanisms. Guo *et al.*<sup>77</sup> further discussed the combustion mechanism of JP-10 molecules. The results show that JP-10 first burns to form free radical pools, and then the resulting free radicals attack JP-10 molecules causing it to decompose and oxidize to form alcohols, ketones and other species. Finally, these species further react with small molecular free radicals to form final products such as  $CO_2$  and  $H_2O$ .

Feng *et al.*<sup>78</sup> studied the reaction process of pyrolysis and oxidation of JP-10 on functionalized graphene sheets (FGS) and

found the reaction path of pyrolysis and oxidation of JP-10 on FGS. As shown in Fig. 4(b), OH on FGS is separated from FGS at first, and then OH participates in the pyrolysis or oxidation of JP-10. Finally, more OH and H radicals are further involved in the reaction to form stable small molecules. The calculation shows that this path greatly reduces the energy barrier of the reaction and accelerates the reaction.

For the sake of environmental protection, renewable biojet fuels have been widely studied recently. Kwon *et al.*<sup>79</sup> and Lele *et al.*<sup>80</sup> have studied the pyrolysis processes of a series of head-to-head (HtH) polycyclic hydrocarbon molecules using a time step of 0.1 fs. The structures of the six molecules are shown in Fig. 5(a). These six molecules can be divided into two categories: one is connected by a C–C bond to two cyclic molecules, and the other is connected by a central four-membered ring to two cyclic molecules. The calculation of kinetic parameters shows that the fuel molecules with central four-membered rings show higher reaction activity. The pyrolysis of the reaction molecules shows that the initial decomposition paths can be divided into two types: (1) central bond breakage and (2) molecular ring-opening reaction. The analysis of the pyrolysis path of HtH polycyclic hydrocarbon molecules shows that small molecular olefins and alkynes constitute the main body of the product, which is different from the pyrolysis products of other fuel molecules. This gives people a more comprehensive understanding of the mechanism of fuel initial pyrolysis. These efforts provide a reference for people to explore the pyrolysis and combustion mechanism of a wider range of new aviation fuels.



Fig. 5 (a) Molecular structure of six HtH polycyclic alkanes;<sup>80</sup> (b) molecular structure of farnesane,  $\alpha$ -farnesene, and  $\beta$ -farnesene;<sup>81</sup> and (c) the initial decomposition path and its proportion of PMT molecules.<sup>82</sup>



Goncalves *et al.*<sup>81</sup> explored the pyrolysis and combustion kinetics and mechanism of three substances, farnesane,  $\alpha$ -farnesene and  $\beta$ -farnesene, which can be used as biojet fuels. The molecular structures of the three species are shown in Fig. 5(b). The analysis shows that the initial path is mainly C–H bond cleavage, accompanied by a small amount of C–C bond breakage. But compared with farnesane, the existence of double bonds in  $\alpha$ -farnesene and  $\beta$ -farnesene increases the molecular reaction activity and accelerates the reaction. The strength of the C–C bond is enhanced by the presence of the double bond, and C–C bond breakage is reduced. In addition, the calculated results of kinetic parameters are verified by experimental data. Wang *et al.*<sup>82</sup> studied the pyrolysis process of *p*-menthane (1-isopropyl-4-methylcyclohexane, PMT) and analyzed the initial decomposition path of PMT. It can be seen from Fig. 5(c) that the cleavage reaction of the isopropyl group and the ring-opening reaction caused by the cleavage of the C–C bond near the isopropyl group are the main reaction pathways. Further analysis shows that all kinds of ring-opening products continue to decompose through  $\beta$ -scission reactions and finally produce a large number of ethylene, propylene and other products. These works can further deepen our understanding of the pyrolysis and combustion mechanisms of high-density aviation fuels.

### 3 Pyrolysis and combustion mechanism of aerospace fuels and energetic additives

Although information about the macroscopic combustion properties of aerospace fuels has been obtained through experiments, the limitations of the experiments themselves prevent people from gaining insight into the atomic-level details of the combustion process of aerospace fuels. However, the emergence of ReaxFF<sup>10</sup> enables people to study the overall mechanism of pyrolysis and combustion of space fuels more intuitively at the micro level. Energetic materials as additives can greatly improve the specific impulse of rocket fuels. The study of their pyrolysis and combustion mechanism can deepen people's understanding of the interaction between energetic materials and aerospace fuels, and further improve the selection of energetic materials and fuels, providing guidance on improving the combustion efficiency of aerospace fuels.

#### 3.1 Pyrolysis and combustion mechanism of aerospace fuels

At present, the widely used aerospace fuels are refined kerosene RP-1, hydrazine, unsymmetrical dimethylhydrazine, nitromethane, liquid hydrogen, triple-base solid propellants and so on. There have been some studies on the pyrolysis or combustion mechanism of these fuels by reactive molecular dynamics.

Han *et al.*<sup>83</sup> studied the pyrolysis process of the RP-1 aerospace kerosene 3-component model and the 24-component alternative model using a time step of 0.1 fs. The results show that there are some differences in the pyrolysis characteristics of these two alternative models. The pyrolysis curve shows that

the 24-component substitution model has higher reactivity than the three-component substitution model. The analysis of the reactivity of the components of the two substitution models shows that the high stability and high content of cycloalkanes in the 3-component substitution model are the reasons for the difference. Further analysis of the two substitution models revealed the differences in reaction paths and products. Compared with the 24-component substitution model, the existence of quaternary carbon in isohexadecane molecules in the 3-component substitution model led to the formation of a large amount of 2-methylpropene. The diversity of cyclic species in the 24-component substitution model made the ring-opening reaction more abundant, resulting in more diolefins and cyclic olefins. Another study<sup>84</sup> on the pyrolysis of the RP-1 aerospace kerosene 24-component substitution model provides information on soot nanoparticle generation. The formation of a soot nanoparticle can be divided into three stages: PAH formation, aggregation nucleation and graphitization to form a soot nanoparticle. The evolution process is shown in Fig. 6. In the first stage, the long carbon chain containing polyalkyne groups forms a large ring, then a bridge is formed within the molecule, and some small rings are formed within the large ring to form a PAH molecule. In the second stage, the side chain of PAH is closed, a bridge bond is generated inside, and the molecules are aggregated into nuclei. In the last stage, the C5/C7 ring is transformed into a six-membered ring to form a soot nanoparticle. These studies have made an effort to evaluate the overall mechanism of the RP-1 fuel substitution model and prevent coking during combustion.

As clean energy, liquid hydrogen is often mixed with liquid oxygen for aerospace fuel. The HO-2011 reaction force field developed by Agrawalla *et al.*,<sup>85</sup> the CHO-2008<sup>15</sup> reaction force field and the HO-2014<sup>21</sup> and CHO-2016<sup>20</sup> reaction force fields improved on the basis of the CHO-2008 reaction force field are all suitable for hydrogen combustion or pyrolysis systems. The pyrolysis process of liquid hydrogen at ultra-high temperature was studied by Kudinov *et al.*,<sup>86</sup> and the results showed that the pyrolysis products and pyrolysis activation energies were consistent with previous studies. Palacios *et al.*<sup>87</sup> studied the combustion of hydrogen in a high-pressure system. The simulation results showed that  $\text{H}_2 + \text{O}_2 \rightarrow \text{H} + \text{HO}_2$  was the most important initial reaction, but further calculations show that collisions between three molecules frequently occur at ultra-high pressures, and the trimolecular reaction  $2\text{O}_2 + \text{H}_2 \rightarrow 2\text{HO}_2$  and  $2\text{O}_2 + \text{H}_2 \rightarrow \text{H} + \text{HO}_2 + \text{O}_2$  may be the new initiation mechanism of  $\text{H}_2$  oxidation. Sun *et al.*<sup>88</sup> studied the mixed combustion of  $\text{H}_2$  and  $\text{CH}_4$  under the action of an electric field. The results show that the consumption rate of  $\text{H}_2$  increases obviously under the action of an external electric field, and the initial reaction time changes. In addition, the addition of an electric field reduces the diversity of free radicals but produces unique species. This study confirms the broad application prospect of ReaxFF in exploring the mechanism of fuel combustion under the action of an external electric field. Bertels *et al.*<sup>89</sup> evaluated the above four reaction force fields that can be used in hydrogen combustion systems based on quantum





Fig. 6 Soot nanoparticle nucleation evolution process.<sup>84</sup>

mechanical methods. The results show that ReaxFF using these reaction force fields is not accurate enough to describe hydrogen combustion systems, and further optimization is needed to better conform to the results of quantum mechanical calculations.

Hydrazine has become a widely used aerospace fuel due to its good energy properties and long-term storage at low temperatures. Zhang *et al.*<sup>90</sup> studied the pyrolysis of bulk hydrazine ( $N_2H_4$ ) and the decomposition of bulk hydrazine over Pt catalysts, and explored the effect of temperature on the pyrolysis process. The results show that bulk hydrazine decomposes to produce  $NH_3$  at lower temperatures, but the initial products change to  $N_2$  and  $H_2$  at higher temperatures. Compared with bulk hydrazine, the catalytic effect of the Pt catalyst reduced the initial decomposition temperature of hydrazine by half. This study further affirms the applicability of ReaxFF. Liu *et al.*<sup>91</sup> studied the combustion process of spontaneous combustion system monomethylhydrazine (MMH) and dinitrogen tetroxide (NTO). Compared with non-spontaneous combustion system ethanol (EtOH) and NTO, the MMH-NTO system showed a higher reaction rate. The initial path analysis of the MMH-NTO system shows that the initial path of pyrolysis of the MMH-NTO system is N-N bond breakage and hydrogen extraction reaction, and further analysis of the product shows that  $NO_2$  is diffused into the fuel to react. This study shows that the fuel decomposition path in the spontaneous combustion system should have a lower reaction energy barrier to achieve rapid reaction, and the oxidant should have a larger diffusion coefficient to achieve more uniform mixing and higher combustion efficiency.

Nitromethane exhibits fine combustion performance and detonation performance. It is often used as aerospace fuel.

There have been some studies<sup>92–94</sup> on its pyrolysis or combustion mechanism using ReaxFF MD. Xu *et al.*<sup>93</sup> studied the pyrolysis of liquid nitromethane in different 2D nanocarbon materials, and the results showed that hybrid carbon atoms and hydroxyl groups participated in the decomposition of nitromethane and promoted the reaction. This work provides insights into the selection of 2D nanocarbon material catalysts for specific fuel pyrolysis or combustion systems. Guo *et al.*<sup>94</sup> studied the improvement of detonation performance of nitromethane by mixing nitromethane and  $NCNO_2$ . The results showed that the Chapman–Jouguet (CJ) temperature, CJ pressure and detonation velocity of the 1 : 1 mixed system were greatly improved. Product analysis showed that the addition of  $NCNO_2$  increased the production of gaseous molecules while reducing the mass of carbon clusters, which caused this change. This work provides a reference for the improvement of detonation performance of nitromethane or other fuels.

Yi *et al.*<sup>95</sup> evaluated the pyrolysis of an RDX modified triple-base solid propellant. Analysis of pyrolysis products shows that carbon clusters react with  $H_2O$  at high temperature to generate more  $H_2$ , and the pyrolysis products are more abundant at high temperature. These results show that the complete combustion of the propellant at higher temperature can be achieved by adding nano-metals and increasing the content of the oxidant, so as to further improve the energy output.

### 3.2 Pyrolysis and combustion mechanism of energetic additives

**3.2.1 Pyrolysis and combustion mechanism of organic energetic additives.** Energetic additives such as high explosives are often added to the propellant to improve fuel combustion



performance. At present, the most commonly used additives are cyclotetramethylene tetranitramine (HMX), 1,3,5-trinitro-1,3,5-triazinane (RDX) and hexanitrohexaazaisowurtzitan (CL-20). The structural formulas of the three molecules are shown in Fig. 7.

**3.2.1.1 Pyrolysis and combustion mechanism of HMX.** HMX has an eight-membered ring nitramine structure, which has good stability and strong explosive power, and can be used as a component of solid rocket propellants. Zhou *et al.*<sup>96</sup> investigated the pyrolysis mechanism of  $\beta$ -HMX crystals at different densities. Studies have shown that  $\beta$ -HMX mainly undergoes intramolecular decomposition at low density, and the initial decomposition paths are N–N bond breakage, C–N bond breakage and HONO elimination. However, at high density, molecular collisions are frequent, and there are more intermolecular retroactive reactions, resulting in O<sub>2</sub>, HO and macromolecular clusters. Zhu *et al.*<sup>97</sup> studied the physicochemical properties and reaction mechanism of HMX nanocrystals at low temperature. The results show that the change of the position and direction of NO<sub>2</sub> groups in HMX will seriously affect the phase transition of HMX. Furthermore, the transition temperature of the  $\beta$  crystal form and  $\delta$  crystal form of HMX nanocrystals is determined by analysis. Meanwhile, it is found that the initial reaction path of HMX nanocrystals at low temperature is the breaking of the C–H bond, and the product at low temperature is the same as that at high temperature. Zhao *et al.*<sup>98</sup> studied the pyrolysis process of nano-AlH<sub>3</sub> and HMX composites. The results show that HMX adsorbs on the particle surface by forming Al–O and Al–N bonds. During the reaction, the cleavage of C–N and N–O bonds is the main pyrolysis path. Due to the attraction of Al to O and N atoms, the initial decomposition path is barrier-free. Further studies show that the temperature and specific impulse of the composite system are higher than those of the HMX system. In another study,<sup>99</sup> the triaminoguanidine glyoxal energetic polymer was added to HMX crystals to obtain QY-HMX. The results showed that the stability of QY-HMX was improved and it did not decompose at low temperature. This study provides a reference for improving the stability of energetic materials.

Zhou *et al.*<sup>100</sup> studied the decomposition process of HMX crystals induced by thermal shock. The results show that the initial decomposition path of HMX crystals is mainly the fracture of the N–N bond, HONO detachment and ring breaking

reaction. In addition, the analysis shows that compression promotes heat conduction, which leads to earlier initial reaction and more intense propagation reaction. Huang *et al.*<sup>101</sup> studied the pyrolysis process of defective  $\beta$ -HMX crystals under thermal shock. The results show that compared with the  $\beta$ -HMX crystal, the impact sensitivity of the defective  $\beta$ -HMX crystal is improved, and there is a high temperature region in the crystal, which leads to the occurrence of the reaction. In addition, the initial reaction paths of defective crystals are N–N bond cleavage and N–O bond cleavage, and the final products are more abundant. He *et al.*<sup>102</sup> studied the catalysis of water in the process of shock explosion of HMX. The results show that water molecules accelerate the oxidation of C atoms by promoting the transfer of oxygen atoms from N to C, as shown in Fig. 8. As a result, the energy barrier for C–N bond breakage is reduced, resulting in rapid cleavage of HMX.

**3.2.1.2 Pyrolysis and combustion mechanism of RDX.** RDX is a kind of energetic additive with good comprehensive performance because of its stable chemical property and great explosive power. In order to understand the combustion properties of RDX, related research studies<sup>103–108</sup> are being carried out. Peng *et al.*<sup>108</sup> studied the pyrolysis process of  $\alpha$ -RDX and its derivatives. The initial decomposition path shows that the first step of the reaction is the breaking of the N–N bond. The difference is that the ring-opening reaction occurs only after the substituents of  $\alpha$ -RDX derivatives are completely removed, while the ring-opening reaction of  $\alpha$ -RDX occurs when there is a nitro group. Further analysis shows that a smaller C/N ratio is beneficial to improve the pyrolysis performance of energetic materials. Zheng *et al.*<sup>107</sup> investigated the effects of solid-phase pyrolysis of RDX and nanosize effects. The results show that the solid-phase pyrolysis of RDX is divided into two stages: solid-dominated and non-condensed. The decomposition reaction randomly occurred inside the RDX during the RDX pyrolysis, and the smaller size nanocrystals exhibited higher decomposition rates. This study furthers our understanding of the complex interactions of the pyrolysis process of energetic crystals. Peng *et al.*<sup>106</sup> have studied the pyrolysis process of the perfect RDX crystal and the RDX crystal with a molecular vacancy under shock. The initial decomposition path shows that the N–N bond breakage occurs at first, then the C–N bond breakage occurs in both crystals, and the possible C–H bond breaks to form HONO.



Fig. 7 Molecular structure of (a) HMX, (b) HMX and (c) CL-20.





Fig. 8 H and OH transport of water in  $\beta$ -HMX.<sup>102</sup> schematic of (a) H and OH transport, (b and c) H transport, and (d) OH transport.

Further comparative analysis showed that the existence of vacancies enhanced the activity of the N–N bond and accelerated the reaction.

The presence of aluminum can increase the temperature of the system. Researchers often add aluminum to energetic materials to achieve more complete combustion. The pyrolysis of aluminum-containing RDX<sup>109–112</sup> is widely studied. Hao *et al.*<sup>109</sup> studied the promoting effect of Al and Al<sub>2</sub>O<sub>3</sub> nanoparticles on the pyrolysis of RDX. The analysis shows that the participation of Al changes the initial path from the unimolecular reaction of N–N bond cleavage to the bimolecular reaction without an energy barrier or with a low energy barrier, which leads to the early decomposition of RDX. Zhao *et al.*<sup>110</sup> studied the decomposition of RDX in the presence of pure aluminum, surface AlN and surface AlO. The results show that RDX adsorbs on the particle surface by forming N–Al and O–Al bonds. In these systems, the initial decomposition path of RDX is the fracture of the N–O bond. In addition, the calculation of the energy barrier shows that the existence of the AlO surface weakens the attraction of the Al atoms in the bulk phase to the O and N atoms in RDX, resulting in the decrease of the catalytic effect of surface AlO on RDX. The study of Li *et al.*<sup>24</sup> shows that the smaller size of AlH<sub>3</sub> can promote the pyrolysis of RDX more thoroughly. These studies provide insights for the further application of active nano-metals in energetic materials.

**3.2.1.3 Pyrolysis and combustion mechanism of CL-20.** CL-20 is a kind of energetic compound with a cage-like polycyclic nitramine structure, which is often used in additives to improve the specific impulse because of its excellent properties. Through some research studies, the pyrolysis and combustion mechanism of CL-20<sup>113–120</sup> have been preliminarily understood.

Ren *et al.*<sup>120</sup> have studied the pyrolysis process of  $\beta$ -CL-20. The results show that the initial decomposition paths of  $\beta$ -CL-20 are (1) the fracture of the N–NO<sub>2</sub> bond and (2) the fracture of the C–N bond. High temperature is beneficial to the first path, but has little effect on the second path. In addition, during the

low-temperature simulation, a bimolecular reaction in which NO<sub>2</sub> molecules take away oxygen occurs (PI-3), and the overall reaction path is shown in Fig. 9. At the same time, further analysis shows that the simulated intermediates and final products are consistent with the experimental results. Wang *et al.*<sup>114,119</sup> discussed the effect of temperature and density on the pyrolysis of  $\epsilon$ -CL-20. It is found that temperature only affects the pyrolysis rate of  $\epsilon$ -CL-20. The increase of temperature leads to the destruction of the  $\epsilon$ -CL-20 structure in advance, but does not affect the reaction path of  $\epsilon$ -CL-20 pyrolysis. The increase of density decreases the frequency of N–NO<sub>2</sub> bond breakage, although the initial reaction rate increases at high density, the activation energy does not change. And large clusters are easy to be formed at high density, thus reducing the number of small molecular products. Han *et al.*<sup>116</sup> explored the effect of particle size on the pyrolysis of  $\epsilon$ -CL-20. It is found that the decrease of particle size promotes the breaking of only the N–NO<sub>2</sub> bond, increases the reaction rate, and promotes the formation of some products at different reaction stages, but does not form a new  $\epsilon$ -CL-20 decomposition path.

Hu *et al.*<sup>121</sup> studied the pyrolysis process of defective  $\epsilon$ -CL-20 at high temperature. They used a time step of 0.1 fs in the simulation. The results show that the main initial path of  $\epsilon$ -CL-20 pyrolysis is the breaking of the N–NO<sub>2</sub> bond. However, the introduction of vacancy defects reduces the proportion of this path and increases the number of ring-opening reactions, and the reactions first occur around the vacancy defects. In addition, vacancy defects decrease the activation energy of the reaction and increase the reaction rate of  $\epsilon$ -CL-20 pyrolysis, which is more obvious at low temperature. Wang *et al.*<sup>117</sup> studied the pyrolysis of  $\epsilon$ -CL-20 under different conditions. The results show that the initial pyrolysis path of  $\epsilon$ -CL-20 at high temperature is mainly the fracture of N–NO<sub>2</sub>, while under high pressure and impact,  $\epsilon$ -CL-20 first causes the separation of NO<sub>2</sub> by forming intramolecular or intermolecular N–O bonds. Mei *et al.*<sup>118</sup> studied the decomposition of CL-20 in the presence of AlH<sub>3</sub>. The analysis shows





Fig. 9 Initial pyrolysis path of the CL-20 molecule.<sup>119</sup>

that CL-20 adsorbs on the surface of  $\text{AlH}_3$  particles by forming Al-O bonds, and then completes the fracture of N- $\text{NO}_2$  bonds. In addition, further results show that the existence of  $\text{AlH}_3$  reduces the activation energy of CL-20 decomposition, increases the release of energy, and increases the formation of gas products. This work provides a reference for exploring the properties of new composite energetic materials.

**3.2.2 Pyrolysis and combustion mechanism of energetic particle additives.** Metals, especially aluminum, have high combustion enthalpy, which can increase the combustion temperature of the system, and aluminum combustion products are harmless and low cost, so they are widely used as fuel additives. An in-depth understanding of the pyrolysis or combustion of aluminum itself,<sup>122-129</sup> energetic materials/aluminum composites<sup>112,130-135</sup> and small molecule/aluminum systems<sup>123,134,136-140</sup> is of great interest.

**3.2.2.1 Pyrolysis and combustion mechanism of Al.** Zeng *et al.*<sup>125</sup> studied the evolution behavior of core-shell Al/ $\text{Al}_2\text{O}_3$  nanoparticles at high temperature. The results show that the diffusion of O atoms in the shell causes the reaction, and the AlO generated at the core is positively charged and migrates to the shell under the action of the electric field formed by the migration of Al and O until the melting electric field of the shell is zero. Chu *et al.*<sup>124</sup> studied the oxidation process of core-shell Al/ $\text{Al}_2\text{O}_3$  nanoparticles in an oxygen atmosphere. The results show that the whole oxidation process can be divided into four stages: preheating, melting, Al nuclear oxidation and moderate shell oxidation. In the second stage, the Al core melts from the

shell junction. At this stage, the core Al diffuses outward, and the core Al diffuses to the oxide layer to be oxidized, releasing heat, which further promotes the melting of the Al core until it melts completely. In the third stage, the inward diffusion of O atoms in the oxide layer and the outward diffusion of Al atoms lead to the rapid oxidation of the Al core. These studies further deepen people's understanding of the ignition and combustion mechanism of Al nanoparticles.

Hao *et al.*<sup>130</sup> studied the evolution behavior of Al nanoparticles (ANPs) in a high temperature environment in the presence of hot 2,4,6-trinitro-1,3,5-triaminobenzene (TATB). The results show that the smaller size of ANPs is beneficial to the occurrence of micro-explosion, which leads to the more complete decomposition of TATB. Moreover, as shown in Fig. 10, the destruction of the core-shell structure is observed in ANPs with an oxide layer, the core Al atoms gushing out achieve rapid oxidation, and rigid Al-O bonds lead to the formation of central voids. On the other hand, in ANPs without an oxide layer, O atoms diffuse inward and gather in ANPs, while C-Al bonds are formed on the surface, which is mainly caused by hypoxia. In addition, it was also found that although the addition of ANPs increased the heat release of the system and played a catalytic role in the pyrolysis of TATB, it also reduced the yield of gas molecules and increased the number of C/Al clusters. Zhao *et al.*<sup>131</sup> have similar conclusions on the pyrolysis of pentaerythritol tetranitrate (PETN) in the presence of ANPs. In this system, the hot spots in PETN originate from the exothermic oxidation of ANPs. ANPs inhibit the production of  $\text{CO}_2$  but promote the formation of  $\text{H}_2\text{O}$ , which is beneficial to



the increase of specific impulse. The difference in the yield of small molecules between the two systems is mainly caused by the difference in energetic substances. These studies have made efforts to further understand the evolution mechanism of ANPs during the pyrolysis of energetic materials.

Dong *et al.*<sup>139</sup> studied the effects of the size of ANPs and the existence of the oxide layer on the reaction of ANPs with water molecules. The results show that when the size of ANPs decreases, the consumption of H<sub>2</sub>O increases, but ANPs are easy to accumulate at high temperature, which will counteract this effect. The existence of the Al oxide layer will reduce the energy release of the system and reduce the production of H<sub>2</sub>, which can be eliminated by partially replacing the oxide layer with AlH<sub>3</sub>. In addition, it is also found that in the pure Al/H<sub>2</sub>O system, the reaction  $3\text{Al} + 2\text{H}_2\text{O} \rightarrow 2\text{AlO} + \text{AlH}_3 + \text{H}$  occurs on the outer surface of the particles, while in the Al/H<sub>2</sub>O system with an oxide layer, the reaction  $4\text{Al} + \text{Al}_2\text{O}_3 \rightarrow 3\text{Al}_2\text{O}$  occurs in the interior of the particles. Chu *et al.*<sup>123</sup> studied the physical and chemical interaction between ANPs and small molecular oxidants. The results show that from melting to oxidation, the chemical adsorption and reaction diffusion of small molecular oxidants are dominant, and the duration of these two stages varies with different types of oxidants. The diffusion analysis of several small molecular oxidants shows that the reaction diffusion rate is positively related to the molecular diffusion coefficient of the oxidant, but negatively related to the binding energy of Al, which leads to the difference of ANP structure in different oxidants. This study reveals the complex interaction between oxidants and ANPs, which provides guidance for the proportion design of different oxidants in the presence of ANPs.

**3.2.2.2 Pyrolysis and combustion mechanism of AlH<sub>3</sub>.** AlH<sub>3</sub> has excellent hydrogen storage performance and a large combustion calorific value. Compared with Al, AlH<sub>3</sub> has lower combustion

temperature and higher gas production. It is a high-energy additive with great potential to replace Al.

Song *et al.*<sup>128</sup> studied the morphology evolution of aluminum hydride nanoparticles (AHNPs) during dehydrogenation and oxidation. They used a time step of 0.1 fs in the simulation. The results show that the evolution of AHNPs involves four stages: sphere, notched sphere, large branch and small string. It is found that the initial reaction originates from the surface dehydrogenation of AHNPs, and then the oxidation reaction takes place. The decomposition reaction caused by heat transfer into the particles leads to the formation and accumulation of hydrogen. When the temperature rises to 1600 K, the oxide layer breaks and the hydrogen overflows, and the morphology evolves into the second stage. With the temperature rising to 3000 K, large branches appear in the further oxidation of the AHNP, and the morphology enters the third stage. When the temperature rises to 3500 K, the AHNP explodes and the morphology evolves into the fourth stage. Zhao *et al.*<sup>127</sup> studied the evolution behavior of pure and core-shell AHNPs in an O<sub>2</sub> atmosphere. The results show that the oxidation of pure AHNPs begins on the surface of the particles and shows a non-uniform distribution. The further oxidation of pure AHNPs is carried out through the outward diffusion of Al and the inward diffusion of O. The core-shell AHNP analysis shows that the oxidation process is caused by the outward diffusion of Al atoms driven by an electric field and then their reaction with O. On the other hand, the phenomenon of micro-explosion appeared in the oxidation process of AHNPs with smaller size, which accelerated the oxidation process. At lower oxygen concentration, the inner diffusion of O atoms and the outer diffusion of core Al result in the formation of a homogeneous Al-O phase. On the other hand, at higher oxygen concentration, the diffusion rate of core Al increases and the center forms a hollow structure.

In-depth understanding of AHNP oxidation in small molecule systems is of great significance for improving propellant

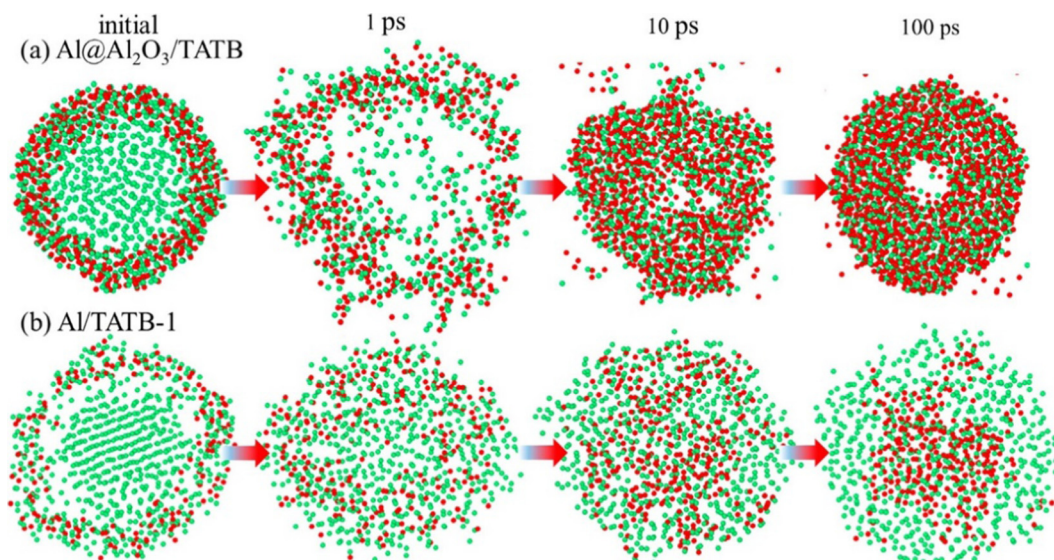


Fig. 10 Morphological evolution of Al atoms in the (a) Al@Al<sub>2</sub>O<sub>3</sub>/TATB and (b) Al/TATB-1 systems at 3000 K.<sup>130</sup>



combustion. Wang *et al.*<sup>134</sup> studied the pyrolysis process of the nitromethane/nano-aluminum hydride (NM/AHNP) composite system. The results show that the addition of AHNPs reduces the energy barrier of pyrolysis, promotes the reaction and increases the release of energy. Further analysis shows that the AHNP oxidizes by capturing O atoms in NM, followed by explosion in the small size AHNP to achieve rapid hydrogen release and oxidation, while further oxidation in the large size AHNP depends on the external diffusion of Al and the internal diffusion of O. Song *et al.*<sup>141</sup> studied the oxidation process of AHNPs in the presence of H<sub>2</sub>O. Studies have shown that AHNPs at low temperature are dominated by dehydrogenation reactions inside and on the surface of the particles. The dehydrogenation on the surface causes the surface rearrangement of Al atoms, while the internal dehydrogenation causes the formation of hydrogen bubbles. When the temperature increases, the internal pressure causes the micro-explosion of AHNPs, which accelerates the reaction. Moreover, the research also reveals the oxidation process of AHNPs, that is, H<sub>2</sub>O is decomposed to form the Al–OH bond, and then O atoms move inward under the action of three Al atoms, resulting in O–H bond cleavage, which leads to the oxidation of Al. This study deepens people's understanding of the overall mechanism of metal hydrides.

#### 4. Challenges for ReaxFF application

ReaxFF MD can dynamically capture the overall morphology of the reaction system and the evolution of different species over time, and then clarify the detailed mechanism of pyrolysis or combustion of the reaction system through analysis, which provides theoretical support for further research. However, a large number of studies have exposed some problems about ReaxFF, such as the deficiency of the QEQ method in describing molecular polarization and the setting of the ground state of high-energy materials by ReaxFF. The QEQ<sup>142</sup> method is insufficient to predict the charge distribution of molecules far from equilibrium; it overestimates the charge flow in the molecule, resulting in the QEQ method describing a much larger molecular polarizability than the true situation. The QTPIE<sup>142</sup> method more comprehensive treatment of the charges inside and outside the molecule compared to the QEQ method allows the method to obtain a lower net charge and a more accurate molecular polarizability, and the addition of such methods is expected to improve the accuracy of the ReaxFF MD calculations. Recently, O'Hearn *et al.*<sup>143</sup> proposed a new charge model, namely ACKS2. Compared with the ReaxFF bond description currently used, this method estimates the Coulomb interaction energy term better, and this improvement is more significant in the ion system. Through the simulation of lithium oxides, they showed that this method can describe the breakage of the molecular covalent bond and ionic bond and the transfer of charge more correctly than the QEQ method. They suggest that this method is more suitable for describing materials similar to ceramics or with high ion bonding. ReaxFF's assumptions about the ground state of energetic materials lead to inaccuracies in ReaxFF's

description of explosive or shock processes in energetic materials. At high thermal temperatures and in the shock state, the electrons of the energetic material may be in an excited state, which is different from the ground state assumption, and this has an impact on the results. This should be noted and improved in subsequent improvements to ReaxFF in relation to excited state chemistry.

In addition, the simulation of ReaxFF in a larger system can fully avoid the influence of accidental factors, and reaction molecules can produce more kinds of intermediates and free radicals through richer reaction pathways. Large-scale<sup>19</sup> reaction molecular dynamics simulation has unique advantages in revealing the overall pyrolysis mechanism of fuel and obtaining overall kinetic information. However, the reaction network in the large-scale reaction system is very complex, and the overall reaction mechanism is difficult to obtain by general methods. The visualization platform VARxMD developed by Liu *et al.*<sup>144</sup> has great advantages in dealing with the details and information of the reaction system. VARxMD completely describes the whole reaction process by combining visual data and visual molecular structure. At present, VARxMD has been applied in many studies<sup>19,145</sup> on fuel pyrolysis. In addition, the large-scale verification of the results of reaction molecular dynamics simulation and experiments is also one of the problems that limit the development of ReaxFF. Due to the limitation of reaction molecular dynamics, most of the current related simulations are carried out at a temperature higher than the experimental temperature. Although the simulation results are qualitatively consistent with the experimental results, they can't be quantitatively compared with the experimental values, especially in terms of kinetic data. The solution of this problem may require the combination of accelerated dynamics and reaction molecular dynamics (such as Accelerated ReaxFF Reactive Dynamics (aARRDyn<sup>21</sup>), Collective Variable-driven Hyperdynamics (CVHD<sup>146</sup>) and ChemTraYzer-TAD<sup>147</sup>), so that the reaction molecular dynamics simulation can reach the same time scale as the experiment at close to the experimental temperature.

#### 5. Conclusion

In this work, the research of ReaxFF MD in the pyrolysis and combustion of aviation/aerospace fuels and energetic additives has been introduced, especially for aviation kerosene model substitutes, high-density aviation fuels, aerospace fuels and energetic additives under various conditions. In addition, we discuss the limitations of ReaxFF applications, particularly in terms of charge, excited state chemistry, verification of simulation results against experiments, and extraction of reaction mechanisms, and point out possible solutions accordingly. In conclusion, ReaxFF has considerable potential to explore the pyrolysis or combustion mechanisms of fuels and energetic materials under extreme conditions.

#### Conflicts of interest

The authors declare no competing financial interest.



## Acknowledgements

This work was financially supported by the Open Research Fund Program of Science and Technology on Aerospace Chemical Power Laboratory (STACPL220221B03), National Natural Science Foundation of China (Grant no. 21978210 and U20A20151) and the National Key R & D Program of China (Grant no. 2018YFA0702403).

## References

- W. Yao, *Acta Mech. Sin.*, 2019, **35**, 1155–1177.
- K. L. Tay, W. B. Yu, F. Y. Zhao and W. M. Yang, *Proc IMechE, Part D: J Automobile Engineering*, 2020, **234**, 303–333.
- P. Dagaut and M. Cathonnet, *Prog. Energy Combust. Sci.*, 2006, **32**, 48–92.
- S. Honnet, K. Seshadri, U. Niemann and N. Peters, *Proc. Combust. Inst.*, 2009, **32**, 485–492.
- A. Violi, S. Yan, E. G. Eddings, A. F. Sarofim, S. Granata, T. Faravelli and E. Ranzi, *Combust. Sci. Technol.*, 2002, **174**, 399–417.
- S. Wang, G. Dai, H. Yang and Z. Luo, *Prog. Energy Combust. Sci.*, 2017, **62**, 33–86.
- E. Huo, S. Zhang, L. Xin, S. Wang, S. Cai, L. Zhang and M. Bai, *Comput. Theor. Chem.*, 2022, **1211**, 113696.
- E. Huo, L. Xin, S. Zhang, C. Liu, S. Wang and L. Zhang, *Process Saf. Environ. Prot.*, 2022, **161**, 603–610.
- Z. Chen, J. Pei, R. Li and F. Xiao, *Constr. Build. Mater.*, 2018, **189**, 695–710.
- A. C. T. van Duin, S. Dasgupta, F. Lorant and W. A. Goddard, *J. Phys. Chem. A*, 2001, **105**, 9396–9409.
- F. Castro-Marciano, A. M. Kamat, M. F. Russo, A. C. T. van Duin and J. P. Mathews, *Combust. Flame*, 2012, **159**, 1272–1285.
- C. Chen, L. Zhao, J. Wang and S. Lin, *Ind. Eng. Chem. Res.*, 2017, **56**, 12276–12288.
- K. Chenoweth, A. C. T. van Duin, S. Dasgupta and W. A. Goddard III, *J. Phys. Chem. A*, 2009, **113**, 1740–1746.
- T. P. Senftle, S. Hong, M. M. Islam, S. B. Kylasa, Y. Zheng, Y. K. Shin, C. Junkermeier, R. Engel-Herbert, M. J. Janik, H. M. Aktulga, T. Verstraelen, A. Grama and A. C. T. van Duin, *npj Comput. Mater.*, 2016, **2**, 15011.
- K. Chenoweth, A. C. T. van Duin and W. A. Goddard, *J. Phys. Chem. A*, 2008, **112**, 1040–1053.
- L. Liu, C. Bai, H. Sun and W. A. Goddard, *J. Phys. Chem. A*, 2011, **115**, 4941–4950.
- X.-M. Cheng, Q.-D. Wang, J.-Q. Li, J.-B. Wang and X.-Y. Li, *J. Phys. Chem. A*, 2012, **116**, 9811–9818.
- Q.-D. Wang, J.-B. Wang, J.-Q. Li, N.-X. Tan and X.-Y. Li, *Combust. Flame*, 2011, **158**, 217–226.
- H. Liu, J. Liang, R. He, X. Li, M. Zheng, C. Ren, G. An, X. Xu and Z. Zheng, *Combust. Flame*, 2022, **237**, 111865.
- C. Ashraf and A. C. T. van Duin, *J. Phys. Chem. A*, 2017, **121**, 1051–1068.
- T. Cheng, A. Jaramillo-Botero, W. A. Goddard and H. Sun, *J. Am. Chem. Soc.*, 2014, **136**, 13467.
- M. Kowalik, C. Ashraf, B. Damirchi, D. Akbarian, S. Rajabpour and A. C. T. van Duin, *J. Phys. Chem. B*, 2019, **123**, 5357–5367.
- S. Cheung, W.-Q. Deng, A. C. T. van Duin and W. A. Goddard, *J. Phys. Chem. A*, 2005, **109**, 851–859.
- C.-F. Li, Z. Mei, F.-Q. Zhao, S.-Y. Xu and X.-H. Ju, *Phys. Chem. Chem. Phys.*, 2018, **20**, 14192–14199.
- H. Zhang, F. Chen, J. Xu, J. Zhang and Y. Han, *Front. Chem. Sci. Eng.*, 2022, **16**, 886–896.
- G. Psafogiannakis and A. C. T. van Duin, *Surf. Sci.*, 2016, **646**, 253–260.
- D. H. Kim, S. J. Kwak, J. H. Jeong, S. Yoo, S. K. Nam, Y. Kim and W. B. Lee, *ACS Omega*, 2021, **6**, 16009–16015.
- B. D. Jensen, A. Bandyopadhyay, K. E. Wise and G. M. Odegard, *J. Chem. Theory Comput.*, 2012, **8**, 3003–3008.
- Y. Han, D. Jiang, J. Zhang, W. Li, Z. Gan and J. Gu, *Front. Chem. Sci. Eng.*, 2016, **10**, 16–38.
- X. Li, M. Zheng, C. Ren and L. Guo, *Energy Fuels*, 2021, **35**, 11707–11739.
- G. Li, F. Zheng, Q. Huang, J. Wang, B. Niu, Y. Zhang and D. Long, *J. Anal. Appl. Pyrolysis*, 2022, **166**, 105620.
- J. Yu, B. Yu and J. Yu, *JASP*, 2020, **35**, 673–681.
- P. Dagaut, A. El Bakali and A. Ristori, *Fuel*, 2006, **85**, 944–956.
- S. Dooley, S. H. Won, M. Chaos, J. Heyne, Y. Ju, F. L. Dryer, K. Kumar, C.-J. Sung, H. Wang, M. A. Oehlschlaeger, R. J. Santoro and T. A. Litzinger, *Combust. Flame*, 2010, **157**, 2333–2339.
- C. Liu, S. Qiu, H. Huang, P. Guo and E. Huo, *Mater. Rev.*, 2019, **33**, 1251–1256.
- E. Wang, J. Ding, Z. Qu and K. Han, *Energy Fuels*, 2018, **32**, 901–907.
- Y. Liu, X. Wei, W. Sun and L. Zhao, *Energy Fuels*, 2021, **35**, 16778–16790.
- L. Liu, H. Xu, Q. Zhu, H. Ren and X. Li, *Chem. Phys. Lett.*, 2020, **760**, 137983.
- W. Zhou, X. Zhang, W. Zhou, L. Yang and Z. Jia, *J. Energy Inst.*, 2022, **102**, 82–91.
- Q.-D. Wang, X.-X. Hua, X.-M. Cheng, J.-Q. Li and X.-Y. Li, *J. Phys. Chem. A*, 2012, **116**, 3794–3801.
- K. M. Bal and E. C. Neyts, *Chem. Sci.*, 2016, **7**, 5280–5286.
- K. M. Bal and E. C. Neyts, *J. Chem. Theory Comput.*, 2015, **11**, 4545–4554.
- Z. Chen, W. Sun and L. Zhao, *J. Phys. Chem. A*, 2017, **121**, 2069–2078.
- Z. Chen, P. Zhao, L. Zhao and W. Sun, *Energy Fuels*, 2017, **31**, 10515–10524.
- D. Kim, J. Martz and A. Violi, *Combust. Flame*, 2014, **161**, 1489–1498.
- K. Narayanaswamy, H. Pitsch and P. Pepiot, *Combust. Flame*, 2016, **165**, 288–309.
- Y. Liu, J. Ding and K.-L. Han, *Fuel*, 2018, **217**, 185–192.
- Y. Dai, W. Zhao, H. Xie, Y. Guo and W. Fang, *J. Anal. Appl. Pyrolysis*, 2020, **145**, 104723.
- Y. Guan, J. Lou, R. Liu, H. Ma and J. Song, *Fuel*, 2020, **261**, 116447.



- 50 H. S. Sim, R. A. Yetter, S. Hong, A. C. T. van Duin, D. M. Dabbs and I. A. Aksay, *Combust. Flame*, 2020, **217**, 212–221.
- 51 L. Xin, C. Liu, Y. Liu, E. Huo, Q. Li, X. Wang and Q. Cheng, *Fuel*, 2020, **275**, 117885.
- 52 H. Hirai, *Chem. Phys.*, 2021, **548**, 111225.
- 53 Y. Liu, G. Li and J. Ding, *Fuel*, 2019, **241**, 273–282.
- 54 M. Wei, S. Wu, Q. Mao, Y. Wang, G. Guo and D. Zhang, *Fuel*, 2020, **275**, 117989.
- 55 Y. Qian, W. Xu, J.-H. Zhan, X. Jia and F. Zhang, *Process Saf. Environ. Prot.*, 2021, **147**, 578–588.
- 56 T. Shou, N. Xu, Y. Li, G. Sun, M. T. Bernards, Y. Shi and Y. He, *Plasma Process.*, 2019, **39**, 863–876.
- 57 M. Duplančić, V. Gomzi, A. Pintar, S. Kurajica and V. Tomašić, *Ceram. Int.*, 2021, **47**, 3108–3121.
- 58 S. Tan, T. Xia, Y. Shi, J. Pfaendtner, S. Zhao and Y. He, *Sci. Rep.*, 2017, **7**, 1710.
- 59 C. D. Fu, Y. He and J. Pfaendtner, *J. Phys. Chem. A*, 2019, **123**, 3080–3089.
- 60 H. Kwon, S. Shabnam, A. C. T. van Duin and Y. Xuan, *Fuel*, 2020, **262**, 116545.
- 61 P. K. Naik, S. Paul and T. Banerjee, *ChemistrySelect*, 2019, **4**, 12996–13005.
- 62 R. Chaudret, A. Bick and X. Krokidis, *Energy Fuels*, 2016, **30**, 6817–6821.
- 63 P. Zhao, S. Han, X. Li, T. Zhu, X. Tao and L. Guo, *Energy Fuels*, 2019, **33**, 7176–7187.
- 64 Y. Wen, C. Jiang, W. Li, Y. Xie, G. Wang and Y. Hou, *CIESC J.*, 2021, **72**, 1100–1106.
- 65 Y. Wen, W. Li, Y. Xie, Z. Qin, M. Gu, T. Wang and Y. Hou, *Environ. Technol.*, 2022, **43**, 2002–2016.
- 66 Y. Liu, X. Wei, W. Sun and L. Zhao, *Ind. Eng. Chem. Res.*, 2021, **60**, 14674–14684.
- 67 C. Ashraf, S. Shabnam, A. Jain, Y. Xuan and A. C. T. van Duin, *Fuel*, 2019, **235**, 194–207.
- 68 S. Han, X. Li, L. Guo, H. Sun, M. Zheng and W. Ge, *Energy Fuels*, 2020, **34**, 11381–11394.
- 69 K.-F. Song, G.-F. Ji, K. M. Kumari and D.-Q. Wei, *Mol. Simul.*, 2018, **44**, 21–33.
- 70 J. Zeng, L. Cao, C.-H. Chin, H. Ren, J. Z. H. Zhang and T. Zhu, *Phys. Chem. Chem. Phys.*, 2020, **22**, 683–691.
- 71 X. Zhang, L. Pan, L. Wang and J.-J. Zou, *Chem. Eng. Sci.*, 2018, **180**, 95–125.
- 72 H. Wang, S. Gong, L. Wang, X. Zhang and G. Liu, *Fuel*, 2019, **239**, 935–945.
- 73 E. Xiu-tian-feng, L. Pan, X. Zhang and J.-J. Zou, *Fuel*, 2020, **276**, 118047.
- 74 H. Wang, B. Zhang, S. Gong, L. Wang, X. Zhang and G. Liu, *Combust. Flame*, 2021, **226**, 163–181.
- 75 W.-H. Kong, Y.-W. Li, J.-B. Wang and X.-Y. Li, *Comput. Theor. Chem.*, 2021, **1200**, 113232.
- 76 S. Wang, Z. Cui, C. Yu and T. Tan, *J. Phys. Chem. A*, 2020, **124**, 6660–6666.
- 77 F. Guo, X. Cheng and H. Zhang, *Combust. Sci. Technol.*, 2012, **184**, 1233–1243.
- 78 M. Feng, X. Z. Jiang, Q. Mao, K. H. Luo and P. Hellier, *Fuel*, 2019, **254**, 115643.
- 79 H. Kwon, A. Lele, J. Zhu, C. S. McEnally, L. D. Pfefferle, Y. Xuan and A. C. T. van Duin, *Fuel*, 2020, **279**, 118548.
- 80 A. Lele, H. Kwon, K. Ganeshan, Y. Xuan and A. C. T. van Duin, *Fuel*, 2021, **297**, 120724.
- 81 R. F. B. Goncalves, B. K. V. Iha, J. A. F. F. Rocco and A. E. Kuznetsov, *Fuel*, 2022, **310**, 122157.
- 82 Y. Wang, S. Gong, H. Wang, L. Li and G. Liu, *J. Anal. Appl. Pyrolysis*, 2021, **155**, 105045.
- 83 S. Han, X. Li, M. Zheng and L. Guo, *Fuel*, 2018, **222**, 753–765.
- 84 S. Han, X. Li, F. Nie, M. Zheng, X. Liu and L. Guo, *Energy Fuels*, 2017, **31**, 8434–8444.
- 85 S. Agrawalla and A. C. T. van Duin, *J. Phys. Chem. A*, 2011, **115**, 960–972.
- 86 A. V. Kudinov, Y. A. Bogdanova and S. A. Gubin, *Phys. At. Nucl.*, 2019, **82**, 1486–1489.
- 87 M. Monge-Palacios and H. Rafatijo, *Phys. Chem. Chem. Phys.*, 2017, **19**, 2175–2185.
- 88 F. Sun and W. Zeng, *Int. J. Hydrogen Energy*, 2020, **45**, 20194–20199.
- 89 L. W. Bertels, L. B. Newcomb, M. Alaghemandi, J. R. Green and M. Head-Gordon, *J. Phys. Chem. A*, 2020, **124**, 5631–5645.
- 90 L. Zhang, A. C. T. v Duin, S. V. Zybin and W. A. Goddard Iii, *J. Phys. Chem. B*, 2009, **113**, 10770–10778.
- 91 Y. Liu, S. V. Zybin, J. Guo, A. C. T. van Duin and W. A. Goddard, *J. Phys. Chem. B*, 2012, **116**, 14136–14145.
- 92 L. Song, F.-Q. Zhao, S.-Y. Xu, X.-H. Ju and C.-C. Ye, *Fuel*, 2021, **303**, 121221.
- 93 J. Xu, Y. Bian, Y. Liu and D. Zhai, *Comput. Mater. Sci.*, 2017, **131**, 126–131.
- 94 D. Guo, S. V. Zybin, W. A. Goddard and Q. An, *J. Phys. Chem. C*, 2020, **124**, 9787–9794.
- 95 J. Yi, Z. Qin, H. Li, F. Zhao, H. Ma and Z. Guo, *J. Mol. Model.*, 2022, **28**, 216.
- 96 T.-T. Zhou, Y.-D. Shi and F.-L. Huang, *Acta Phys.-Chim. Sin.*, 2012, **28**, 2605–2615.
- 97 S. Zhu and W. Zhu, *J. Nanopart. Res.*, 2020, **22**, 362.
- 98 Y. Zhao, Z. Mei, F.-Q. Zhao, S.-Y. Xu and X.-H. Ju, *ACS Omega*, 2020, **5**, 23193–23200.
- 99 H.-R. Zhang, Z.-H. Xue, X. Fu, J.-P. Liu, X. Qi and Q.-L. Yan, *Fuel*, 2022, **324**, 124646.
- 100 T. Zhou, H. Song, Y. Liu and F. Huang, *Phys. Chem. Chem. Phys.*, 2014, **16**, 13914–13931.
- 101 X. Huang, Z. Qiao, X. Dai, K. Zhang, M. Li, G. Pei and Y. Wen, *J. Appl. Phys.*, 2019, **125**, 195101.
- 102 Z.-H. He, J. Chen, Q. Wu and G.-F. Ji, *RSC Adv.*, 2016, **6**, 93103–93110.
- 103 Y. Zhang, H. Liu, Z. Yang, Q. Li and Y. He, *ACS Omega*, 2019, **4**, 8031–8038.
- 104 J. Meng, S. Zhang, R. Gou, Y. Chen, Y. Li, M. Chen and Z. Li, *J. Mol. Model.*, 2020, **26**, 245.
- 105 C. Deng, J. Liu, X. Xue, X. Long and C. Zhang, *J. Phys. Chem. C*, 2018, **122**, 27875–27884.
- 106 Y. J. Peng, S. Sun, W. N. Liu and Y. H. Liu, *Acta Phys. Sin.*, 2021, **70**, 158202.



- 107 K. Zheng, Y. Wen, B. Huang, J. Wang, J. Chen, G. Xie, G. Lv, J. Liu, Z. Qiao and G. Yang, *Phys. Chem. Chem. Phys.*, 2019, **21**, 17240–17252.
- 108 Q. Y. Li-Juan Peng, J.-B. Wang, Z.-R. Li, Q. Zhu and X.-Y. Li, *Acta Phys.-Chim. Sin.*, 2017, **33**, 745–754.
- 109 W. Hao, L. Niu, R. Gou and C. Zhang, *J. Phys. Chem. C*, 2019, **123**, 14067–14080.
- 110 Y. Zhao, F.-Q. Zhao, S.-Y. Xu and X.-H. Ju, *Comput. Mater. Sci.*, 2020, **177**, 109556.
- 111 N. Wang, J. Peng, A. Pang, T. He, F. Du and A. Jaramillo-Botero, *J. Phys. Chem. C*, 2017, **121**, 14597–14610.
- 112 Z. Mei, Q. An, F.-Q. Zhao, S.-Y. Xu and X.-H. Ju, *Phys. Chem. Chem. Phys.*, 2018, **20**, 29341–29350.
- 113 F. Wang, L. Chen, D. Geng, J. Lu and J. Wu, *J. Phys. Chem. C*, 2019, **123**, 23845–23852.
- 114 F. Wang, L. Chen, D. Geng, J. Wu, J. Lu and C. Wang, *J. Phys. Chem. A*, 2018, **122**, 3971–3979.
- 115 J. Zhang and W. Guo, *J. Phys. Chem. A*, 2022, **126**, 286–295.
- 116 Q. Han and W. Zhu, *Chem. Phys. Lett.*, 2020, **761**, 138067.
- 117 F. Wang, L. Chen, D. Geng, J. Lu and J. Wu, *Phys. Chem. Chem. Phys.*, 2020, **22**, 23323–23332.
- 118 Z. Mei, C.-F. Li, F.-Q. Zhao, S.-Y. Xu and X.-H. Ju, *J. Mater. Sci.*, 2019, **54**, 7016–7027.
- 119 F. Wang, L. Chen, D. Geng, J. Lu and J. Wu, *Phys. Chem. Chem. Phys.*, 2018, **20**, 22600–22609.
- 120 C.-X. Ren, X.-X. Li and L. Guo, *Acta Phys. -Chim. Sin.*, 2018, **34**, 1151–1162.
- 121 J. Hu, Q. Gan, C. Feng, C. Li, S. Zhu and N. Cheng, *J. Mater. Eng.*, 2021, **29**, 482–491.
- 122 B. Wu, F. C. Wu, Y. B. Zhu, A. M. He and H. A. Wu, *J. Appl. Phys.*, 2019, **126**, 144305.
- 123 Q. Chu, B. Shi, L. Liao, X. Zou, K. H. Luo and N. Wang, *J. Phys. Chem. C*, 2020, **124**, 3886–3894.
- 124 Q. Chu, B. Shi, L. Liao, K. H. Luo, N. Wang and C. Huang, *J. Phys. Chem. C*, 2018, **122**, 29620–29627.
- 125 H. Zeng, X. Cheng, C. Zhang and Z. Lu, *J. Phys. Chem. C*, 2018, **122**, 9191–9197.
- 126 G. Li, L. Niu, W. Hao, Y. Liu and C. Zhang, *Combust. Flame*, 2020, **214**, 238–250.
- 127 Y. Zhao, D. X. Ma, Z. Mei, F. Q. Zhao, S. Y. Xu and X. H. Ju, *Int. J. Energy Res.*, 2022, **46**, 11079–11091.
- 128 L. Song, F.-Q. Zhao, S.-Y. Xu and X.-H. Ju, *Appl. Surf. Sci.*, 2020, **519**, 146249.
- 129 Q. Chu, X. Chang and D. Chen, *Combust. Flame*, 2022, **237**, 111739.
- 130 W. Hao, G. Li, L. Niu, R. Gou and C. Zhang, *J. Phys. Chem. C*, 2020, **124**, 10783–10792.
- 131 Y. Zhao, Z. Mei, F.-Q. Zhao, S.-Y. Xu and X.-H. Ju, *Appl. Surf. Sci.*, 2021, **563**, 150296.
- 132 Y. Jiang, S. Deng, S. Hong, S. Tiwari, H. Chen, K.-I. Nomura, R. K. Kalia, A. Nakano, P. Vashishta, M. R. Zachariah and X. Zheng, *ACS Appl. Mater. Interfaces*, 2020, **12**, 7451–7458.
- 133 S. Huang, S. Hong, Y. Su, Y. Jiang, S. Fukushima, T. M. Gill, N. E. D. Yilmaz, S. Tiwari, K.-I. Nomura, R. K. Kalia, A. Nakano, F. Shimojo, P. Vashishta, M. Chen and X. Zheng, *Combust. Flame*, 2020, **219**, 467–477.
- 134 X.-K. Wang, Y. Zhao, F.-Q. Zhao, S.-Y. Xu and X.-H. Ju, *J. Mol. Graphics Modell.*, 2021, **108**, 107987.
- 135 L. Song, F.-Q. Zhao, S.-Y. Xu and X.-H. Ju, *Phys. Chem. Chem. Phys.*, 2021, **23**, 11886–11892.
- 136 R.-K. Dong, Z. Mei, F.-Q. Zhao, S.-Y. Xu and X.-H. Ju, *Int. J. Hydrogen Energy*, 2021, **46**, 1234–1245.
- 137 R.-K. Dong, Z. Mei, S.-Y. Xu, F.-Q. Zhao, X.-H. Ju and C.-C. Ye, *Int. J. Hydrogen Energy*, 2019, **44**, 19474–19483.
- 138 Y. Zhao, D.-X. Ma, F.-Q. Zhao, S.-Y. Xu and X.-H. Ju, *Appl. Surf. Sci.*, 2022, **586**, 152777.
- 139 R.-K. Dong, Z. Mei, F.-Q. Zhao, S.-Y. Xu and X.-H. Ju, *RSC Adv.*, 2019, **9**, 41918–41926.
- 140 L. Song, Z. Mei, S.-Y. Xu, F.-Q. Zhao and X.-H. Ju, *J. Am. Ceram. Soc.*, 2022, **105**, 1343–1357.
- 141 L. Song, F.-Q. Zhao, S.-Y. Xu, C.-C. Ye and X.-H. Ju, *Mater. Today Commun.*, 2021, **26**, 101804.
- 142 J. Chen and T. J. Martinez, *Chem. Phys. Lett.*, 2007, **438**, 315–320.
- 143 K. A. O'Hearn, M. W. Swift, J. L. Liu, I. Magoulas, P. Picuch, A. C. T. van Duin, H. M. Aktulga and Y. Qi, *J. Chem. Phys.*, 2020, 153.
- 144 J. Liu, X. Li, L. Guo, M. Zheng, J. Han, X. Yuan, F. Nie and X. Liu, *Comput. Appl. Chem.*, 2014, **31**, 641–647.
- 145 M. Zheng, Z. Wang, X. Li, X. Qiao, W. Song and L. Guo, *Fuel*, 2016, **177**, 130–141.
- 146 S. Fukuhara, K. M. Bal, E. C. Neyts and Y. Shibuta, *Comput. Mater. Sci.*, 2020, **177**, 109581.
- 147 L. Krep, I. S. Roy, W. Kopp, F. Schmalz, C. Huang and K. Leonhard, *J. Chem. Inf. Model.*, 2022, **62**, 890–902.

